scientific reports

Check for updates

OPEN

Quantitative evaluation of metal artifact reduction in CBCT under varying exposure modes and rod orientations

Gyu-Dong Jo[1], Chul-Wan Park[1], Kug Jin Jeon[1,2] & Sang-Sun Han[1,2]✉

This study aimed to quantitatively evaluate the efficacy of a metal artifact reduction (MAR) algorithm in cone-beam computed tomography (CBCT) under varying exposure modes and metal rod orientations using a standardized evaluation method. A SEDENTEXCT IQ phantom was scanned with a CBCT system under three exposure modes (standard, low-dose, ultra-low-dose) and two rod orientations (horizontal, vertical), with the MAR algorithm activated and deactivated. Artifact areas were quantified from binarized images based on a thresholding method that distinguished artifact-affected regions from the background. The percentage reduction in metal artifacts was calculated by comparing scans acquired with and without MAR activation. Statistical analyses were conducted to assess differences across conditions. The MAR algorithm significantly reduced metal artifacts under all tested conditions ($P < 0.05$), with reductions of 61.5% in the standard mode, 73.6% in the low-dose mode, and 80.3% in the ultra-low-dose mode. By rod orientation, artifact reduction was 63.3% for the horizontal orientation and 80.7% for the vertical orientation. These results confirm the consistent effectiveness of the MAR algorithm across different acquisition settings. The proposed standardized evaluation method provides a reproducible framework for objectively assessing MAR performance and supporting its clinical integration.

Keywords Cone-beam computed tomography, Artifacts, Image processing, computer-assisted, Phantoms, imaging

Cone-beam computed tomography (CBCT) has become an indispensable tool in dental and maxillofacial imaging due to its lower radiation exposure, smaller equipment footprint, and cost-effectiveness compared to multidetector computed tomography (MDCT). However, one significant limitation of CBCT is the presence of metal artifacts caused by dental restorations, implants, or orthodontic appliances. These artifacts appear as streaks or dark and bright regions that degrade image quality, obscure critical anatomical details, and complicate both diagnosis and treatment planning.

To mitigate these challenges, various metal artifact reduction (MAR) algorithms have been developed for CBCT systems. MAR techniques range from projection-based interpolation methods to advanced approaches such as iterative reconstruction and deep learning-based algorithms[1–5]. These methods have demonstrated promising results in reducing artifacts and improving image clarity. However, the effectiveness of MAR algorithms can vary depending on factors such as metal type, artifact complexity, and imaging protocols, making their clinical utility inconsistent[6].

While qualitative improvements in image quality have been well documented, quantitative assessments of MAR algorithms remain limited. Existing studies often suffer from methodological shortcomings, such as using custom-made phantoms or evaluating only arbitrarily selected regions of interest (ROIs), rather than the entire artifact-affected area[3,5,7]. These inconsistencies make it difficult to compare MAR algorithm performance across studies and highlight the need for a standardized and objective evaluation method.

In this study, we aimed to quantitatively evaluate the effectiveness of a MAR algorithm using a standardized quality assurance phantom recommended by SEDENTEXCT, a project for establishing quality assurance in CBCT imaging. Specifically, the study examined the MAR performance across three CBCT exposure modes: standard, low-dose, and ultra-low-dose, as well as two metal rod orientations, horizontal and vertical.

[1]Department of Oral and Maxillofacial Radiology, Yonsei University College of Dentistry, Seoul, Republic of Korea. [2]Oral Science Research Center, Yonsei University College of Dentistry, Seoul, Republic of Korea. ✉email: SSHAN@yuhs.ac

Materials and methods

This in vitro study quantitatively assessed the effectiveness of a MAR algorithm in CBCT. Scans were performed using a CBCT system (T2 Plus; Osstem Implant Co., Ltd., Seoul, Korea) equipped with an X-ray tube, an IGZO-type flat panel detector, and a deep learning-based MAR algorithm. The detector has a native pixel size of 98 µm, with a detector matrix of 1628 × 1628, 16-bit depth, and a frame rate of 33 frames per second. The gantry is rotating type, with a source-to-detector distance of 656.7 mm and a source-to-object distance of 409.7 mm. The system performs a 360° rotational scan and acquires 706 projections per scan using a circular (half-pan) acquisition trajectory.

The CBCT scans were performed in three exposure modes (standard, low-dose, and ultra-low-dose) with constant parameters, including a 15 × 9 cm^2 field of view, 95 kV tube voltage, and 200 µm voxel size. Tube current, exposure time, and binning mode were adjusted for each mode. Scans were performed with the MAR algorithm both deactivated (MAR off) and activated (MAR on), resulting in six distinct scanning conditions. To minimize variability and ensure statistical reliability, each condition was repeated eight times. The detailed scanning parameters are provided in Table 1.

Image reconstruction was performed using a filtered back-projection algorithm based on the Feldkamp-Davis-Kress (FDK) method. High-pass filtering and pixel-driven back projection were applied, followed by post-processing using edge-enhancing denoising and adaptive sharpening filters. Beam-hardening correction is integrated into the standard reconstruction pipeline of the T2 Plus CBCT system and applied automatically during image reconstruction.

The MAR algorithm used in this study, described as "deep learning-based" by the manufacturer, is a proprietary component of the T2 Plus system. According to the manufacturer's documentation, it integrates a GAN-based unsupervised data labeling module and a CNN-based supervised metal segmentation step. Artifact correction is subsequently performed using a projection-domain correction algorithm during post-acquisition reconstruction. The algorithm operates automatically during post-acquisition reconstruction.

A SEDENTEXCT IQ phantom (Leeds Test Objects Ltd., Boroughbridge, UK) was used for the quantitative assessment of metal artifacts. This cylindrical polymethyl methacrylate (PMMA) phantom (diameter: 160 mm; density: 1.20 g/cm^3) includes test inserts designed to evaluate metal artifacts, contrast resolution, and pixel intensity. For this study, the metal artifact inserts containing three titanium rods (diameter: 5.0 mm) embedded in PMMA were utilized. While the exact alloy composition was not specified by the manufacturer, a density of approximately 4.5 g/cm^3 was assumed based on commonly used materials such as commercially pure titanium (CP-Ti) or Ti-6Al-4 V. The rods are fixed within the phantom in both horizontal (parallel to the radius) and vertical (perpendicular to the radius) orientations. These orientations are simultaneously present within the scan volume, as determined by the phantom's design. This configuration reflects clinically relevant conditions and was used consistently across all scans. The phantom was centrally aligned within the scanner's field of view in accordance with the manufacturer's guidelines. Figure 1 shows the phantom setup, and the image was captured by the authors during the experiment.

For each scan, six representative axial slices were selected for quantitative analysis: one reference slice from the homogeneous PMMA layer and five test slices from the metal artifact layer. Each layer consisted of 85 axial slices. The central slice of each layer was identified, and in the metal artifact layer, two additional slices were selected at equal intervals above and below the central point to yield five test slices.

The selected slices were quantitatively analyzed using ImageJ software (version 1.54 g; NIH, Bethesda, MD, USA) as follows (Fig. 2):

1. *ROI selection*: To measure extent of metal artifacts, circular ROIs with a diameter of 32 mm were placed on specific axial slices of each CBCT scan. In the homogeneous PMMA layer, which does not contain any metal, one central ROI was drawn to serve as a reference. This region was used to define the pixel value distribution expected from normal and artifact-free PMMA. In each of the five slices from the metal artifact layer, two ROIs were placed—one over the horizontally oriented titanium rod and the other over the vertically oriented titanium rod. These ROIs were used to assess the degree of image distortion caused by metal.
2. *Threshold calculation*: To define the pixel value range that reflects normal PMMA, the mean and standard deviation (SD) of pixel values were calculated from the reference ROI. Using these values, we defined a reference pixel value range as:

$$Reference\ pixel\ value\ range = [mean - 3 \times SD,\ mean + 3 \times SD]$$

Mode	MAR	FOV (cm^2)	Voxel size (µm)	Tube voltage (kV)	Tube current (mA)	Exposure time (s)	DAP (µGy × m^2)
Standard	Off	15 × 9	200	95	6	22	238.7
	On						
Low-dose	Off	15 × 9	200	95	6	10	111.4
	On						
Ultra-low-dose	Off	15 × 9	200	95	3	10	53.3
	On						

Table 1. CBCT scanning protocols. *MAR* metal artifact reduction, *FOV* field of view, *DAP* dose-area product.

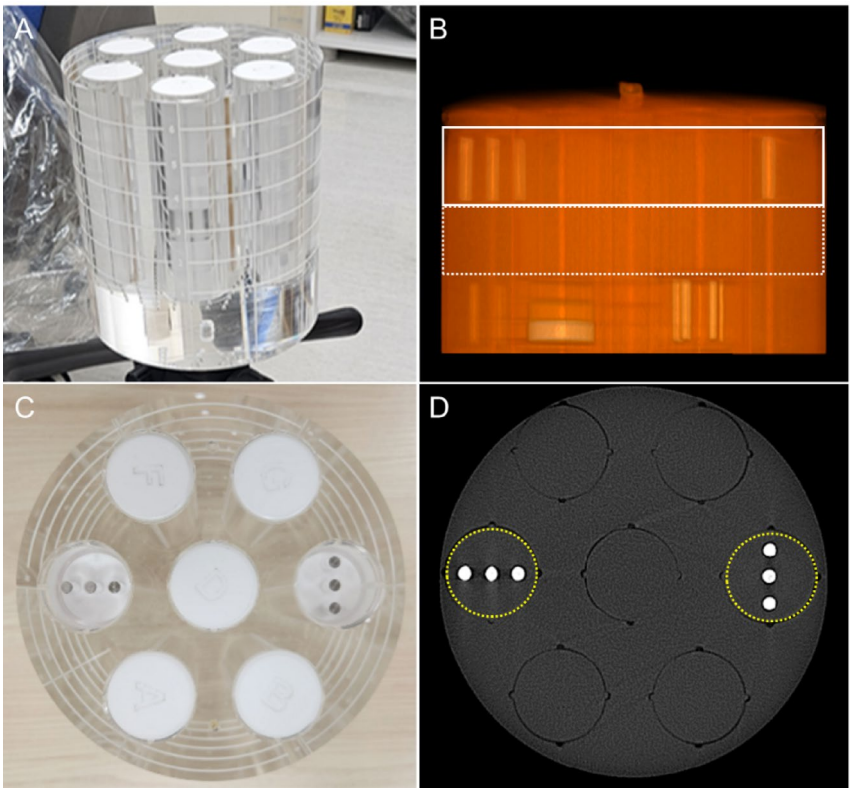

Fig. 1. Phantom setup and region of interest (ROI) placement for metal artifact evaluation. (**A**) Photograph of the SEDENTEXCT IQ phantom used for standardized evaluation of metal artifacts in cone-beam computed tomography (CBCT). (**B**) CBCT projection image indicating the metal artifact evaluation layer (white solid box) and the homogeneous background layer made of polymethyl methacrylate (PMMA), which was used as a reference (white dotted box). (**C**) Cross-sectional photograph of the phantom showing the fixed configuration of three titanium rods positioned in horizontal and vertical orientations. (**D**) Axial CBCT slice used for analysis. Circular regions of interest (yellow dotted circles) were placed over the horizontal and vertical rods to measure the extent of artifact based on pixel value deviations from the PMMA reference.

Pixel values within this range were assumed to be unaffected by artifacts, while values outside the range were considered distorted by metal artifacts or associated with the metal itself.

3. *Binarization:* The reference range was applied to the ROIs in the five test slices to classify each pixel based on its pixel value. Pixels were assigned to one of two categories:

$$White\ (unaffected\ PMMA) : pixel\ values\ within\ the\ reference\ range$$

$$Black\ (metal\ or\ artifacts) : pixel\ values\ outside\ the\ reference\ range$$

This binarization process generated a binary (black-and-white) image, in which metal and artifact-affected areas were clearly visualized as black.

4. *Artifact area calculation:* In the binarized images, black pixels included both metal-induced artifacts and the actual area occupied by the titanium rods. To measure only the artifact, we subtracted the known cross-sectional area of the three titanium rods from the total black pixel area in each ROI:

$$Artifact\ area = (ROI\ area \times proportion\ of\ black\ pixels) - metal\ rod\ area$$

The ROI area was fixed at 804.32 mm^2, and the metal rod area was 58.9 mm^2, corresponding to the three rods embedded in the phantom. This correction allowed us to isolate and accurately quantify only the artifact-affected region. The artifact areas from the five test slices were then averaged to represent the result for each scanning condition.

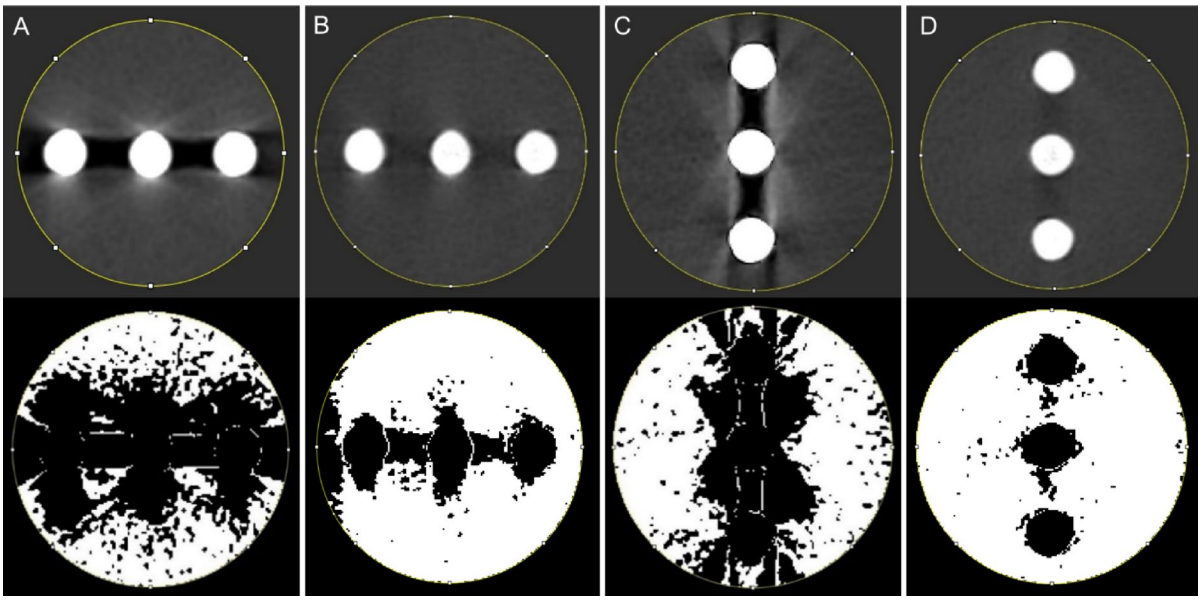

Fig. 2. Representative cone-beam computed tomography (CBCT) images and threshold-based binarization used for metal artifact quantification. Top row: original axial CBCT images with circular regions of interest (ROIs) placed over horizontally and vertically oriented titanium rods. These ROIs correspond to the locations indicated in Fig. 1D. Bottom row: Corresponding binarized images generated by applying thresholding based on the pixel value distribution of the homogeneous polymethyl methacrylate (PMMA) reference region. Pixels within the defined range (mean ± 3 standard deviations) were classified as unaffected PMMA (white), while those outside the range were classified as metal or artifact regions (black). (**A**, **B**) Low-dose mode, horizontally oriented rods, with metal artifact reduction (MAR) deactivated and activated, respectively. (**C**, **D**) Low-dose mode, vertically oriented rods, with MAR deactivated and activated, respectively.

5. *Percent reduction calculation*: To assess how effectively the MAR algorithm reduced artifacts, we calculated the percentage reduction in artifact area by comparing the averaged values with and without MAR enabled:

$$Percent\ reduction\,(\%) = \frac{Artifact\ area\,(MAR\ off) - Artifact\ area(MAR\ on)}{Artifact\ area(MAR\ off)} \times 100$$

This value provided a standardized, quantitative measure of the MAR algorithm's performance under various exposure conditions and rod orientations.

All statistical analyses were performed using SPSS software (version 25.0; IBM Corp., Armonk, NY, USA). Artifact areas with the MAR algorithm deactivated and activated were compared using the Wilcoxon signed-rank test. Differences among exposure modes (standard, low-dose, and ultra-low-dose) and between rod orientations (horizontal and vertical) were analyzed using the Kruskal–Wallis test, followed by the Mann–Whitney U test for pairwise comparisons where appropriate. Statistical significance was defined as $P < 0.05$.

This study did not involve human participants or live vertebrates/invertebrates. Instead, it utilized an in vitro experimental design with a standardized phantom model (SEDENTEXCT IQ phantom). As such, ethical approval and informed consent requirements are not applicable. The study adhered to all relevant guidelines for in vitro research and imaging protocols.

Results

A total of 240 axial images were analyzed, with 120 images obtained with the MAR algorithm deactivated (MAR off) and 120 images processed with the algorithm activated (MAR on). The evaluation included different exposure modes (standard, low-dose, and ultra-low-dose) and rod orientations (horizontal and vertical).

Figure 3 presents representative CBCT images that qualitatively demonstrate how exposure mode and rod orientation affect the severity of metal artifacts. These visual observations are substantiated by quantitative measurements of artifact area and percent reduction, as summarized in Table 2.

Evaluation of metal artifact reduction across exposure modes

The MAR algorithm significantly reduced artifact areas across all exposure modes (Fig. 4A). Percent reduction values were 61.5% in the standard dose, 73.6% in the low-dose, and 80.3% in the ultra-low-dose mode, with the highest reduction observed in the ultra-low-dose mode (Fig. 4B).

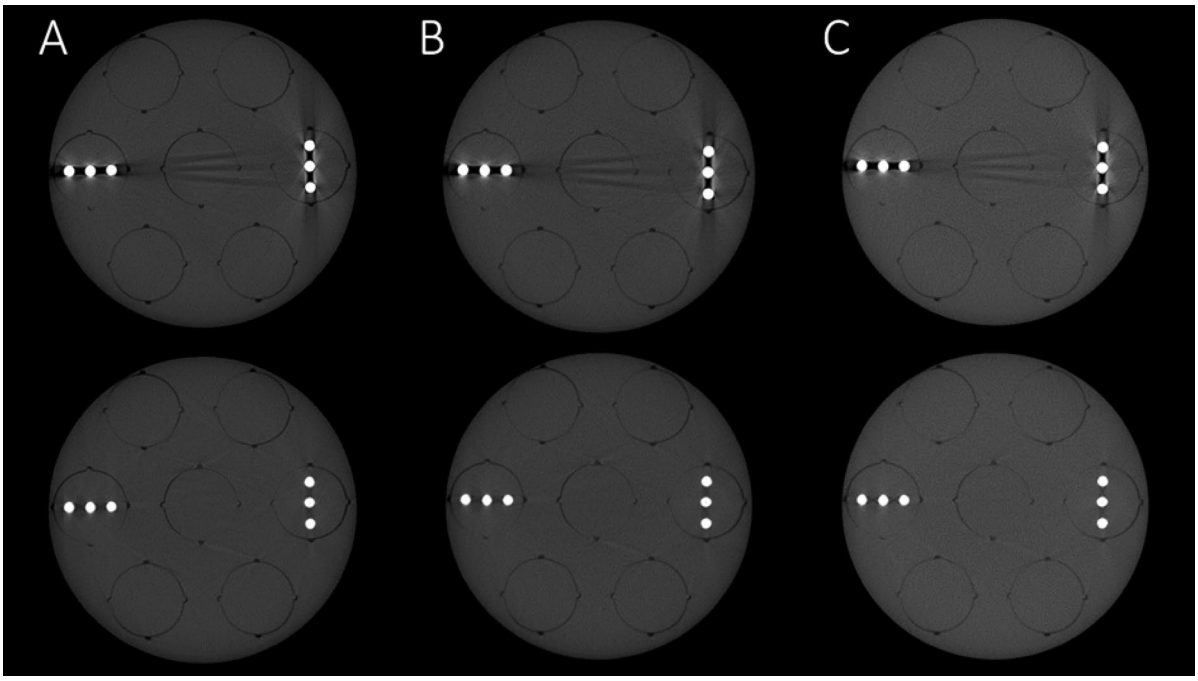

Fig. 3. Representative axial cone-beam computed tomography (CBCT) images of the SEDENTEXCT IQ phantom acquired under varying exposure conditions. Top row: images obtained with the metal artifact reduction (MAR) algorithm deactivated. Bottom row: corresponding images with the MAR algorithm activated. (**A**) Standard mode, (**B**) Low-dose mode, (**C**) Ultra-low-dose mode. Horizontally and vertically oriented titanium rods are positioned on the right and left sides of each image, respectively.

Conditions	MAR off (mm^2)	MAR on (mm^2)	Percent reduction (%)
Overall	317.39 ± 60.60	92.40 ± 55.27	70.9
By exposure mode			
Standard	358.28 ± 40.28	137.83 ± 57.16	61.5
Low-dose	331.59 ± 50.78	87.66 ± 41.45	73.6
Ultra-low-dose	262.30 ± 44.01	51.72 ± 21.61	80.3
By rod orientation			
Horizontal	357.82 ± 45.78	131.45 ± 50.26	63.3
Vertical	276.96 ± 44.53	53.36 ± 23.09	80.7

Table 2. Measured artifact area and percentage reduction across conditions. Measured artifact areas are presented as mean ± standard deviation. Percent reduction was calculated as: (artifact area of MAR off − artifact area of MAR on)/artifact area of MAR off × 100. *MAR* metal artifact reduction, *off* deactivated, *on* activated.

Evaluation of metal artifact reduction based on rod orientation

The MAR algorithm significantly reduced artifact areas regardless of rod orientation (Fig. 5A). Percent reduction values were 63.3% in the horizontal rod orientation and 80.7% in the vertical rod orientation, with the greater reduction observed in the vertical orientation (Fig. 5B).

Discussion

This study quantitatively evaluated the performance of a proprietary MAR algorithm implemented in a CBCT system using a standardized quality assurance phantom. The results showed an overall reduction in artifact area of approximately 70%, with significant improvements observed across all exposure settings and metal rod orientations. These findings support the feasibility of the proposed threshold-based quantification method and demonstrate the artifact-reducing potential of the tested MAR algorithm in CBCT imaging.

The MAR algorithm demonstrated consistent artifact reduction across all exposure settings, with percent reductions of 61.5%, 73.6%, and 80.3% in the standard, low-dose, and ultra-low-dose modes, respectively. At first glance, the trend of greater reduction at lower exposures may appear counterintuitive, as reduced photon flux is typically associated with increased image noise and more pronounced artifacts. However, this observation reflects a characteristic of our threshold-based quantification method rather than an actual improvement in image quality. In our approach, artifacts were defined as pixels with intensity values outside the range of mean ± 3

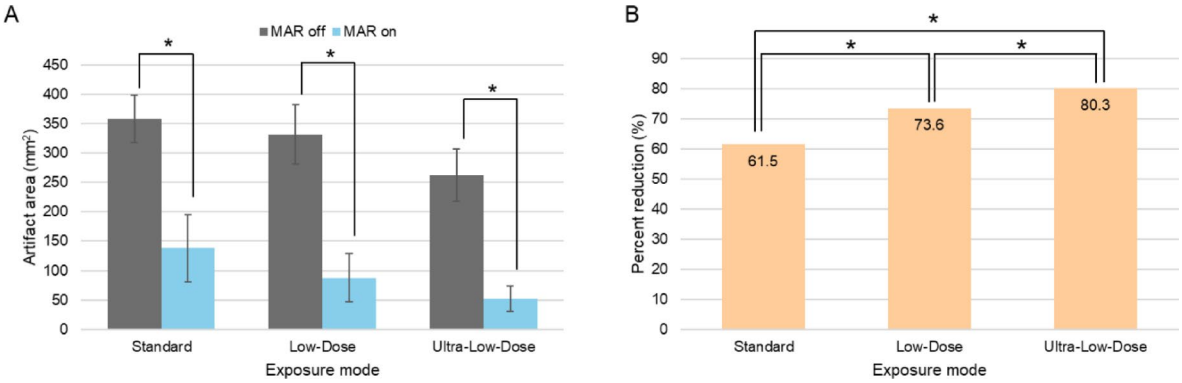

Fig. 4. (**A**) Measured artifact areas (mm^2) across exposure modes with MAR deactivated and activated. Error bars indicate standard deviations (*$P < 0.05$, Wilcoxon signed-rank test). (**B**) Percent reduction in artifact areas across exposure modes with MAR activated. (*$P < 0.05$, Kruskal–Wallis test followed by Mann–Whitney U test).

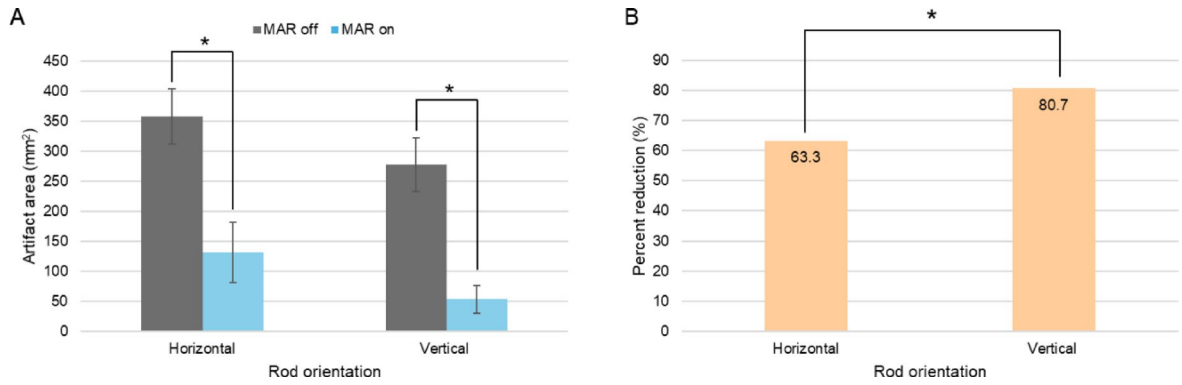

Fig. 5. (**A**) Measured artifact areas (mm^2) according to rod orientation with MAR deactivated and activated. Error bars indicate standard deviations (*$P < 0.05$, Wilcoxon signed-rank test). (**B**) Percent reduction in artifact areas by rod orientation with MAR activated (*$P < 0.05$, Mann–Whitney U test).

standard deviations (SD) of a homogeneous PMMA region. Increased noise at lower exposures elevates the SD, thereby broadening the threshold range and reducing the number of pixels classified as artifacts. For example, the threshold interval expanded from approximately 220–550 in the standard-dose mode to 480–1090 in the ultra-low-dose mode. As a result, even if the images appear noisier, fewer pixels exceed the threshold and are included in the artifact area calculation. The higher percent reduction seen at lower doses is thus a mathematical outcome of the evaluation formula: when the denominator (artifact area before MAR) is smaller, a similar or modest absolute reduction (numerator) results in a higher percent change. This highlights the importance of interpreting percent-based metrics in the context of the measurement method rather than assuming improved algorithmic performance at lower exposure levels.

The orientation of metal rods also had a significant impact on MAR performance, with greater artifact reduction observed when the rods were positioned vertically (80.7%) compared to horizontally (63.3%). This difference can be explained by the geometric nature of artifacts relative to the imaging plane: vertically oriented rods generate localized and distinct artifacts that are easier to detect, whereas horizontally oriented rods produce broader, more diffuse artifacts. Although previous studies have suggested that the position of metal objects within the field of view does not significantly affect MAR performance, our findings emphasize that metal orientation plays a critical role in algorithm efficacy[8]. From a clinical perspective, these results suggest that optimizing patient positioning or adjusting the orientation of metallic implants during CBCT imaging can further enhance the MAR algorithm's performance. Incorporating such strategies into clinical practice could improve image quality, particularly in cases with extensive metal artifacts, thereby supporting more accurate diagnoses and treatment planning.

The threshold-based methodology proposed in this study offers a reproducible and objective framework for quantifying metal artifacts in CBCT images. By defining artifacts based on deviation from the intensity distribution of a homogeneous reference region, our method reflects the net visible impact of artifacts under clinically relevant conditions. This approach does not attempt to isolate individual physical causes of artifact formation—such as scatter, photon starvation, or beam hardening—but instead captures their cumulative effect as they appear in reconstructed images[9,10].

Since MAR algorithms were first introduced in the 1980s, several approaches have been developed and refined to address metal-induced artifacts in CBCT imaging[11,12]. First, projection-based methods, such as inpainting and interpolation, work by estimating missing or distorted data in metal-affected areas, significantly reducing streak artifacts in the projection domain before image reconstruction[3,13,14]. Second, iterative reconstruction techniques iteratively refine the reconstruction process by comparing reconstructed images to the original projections, enabling more accurate artifact correction while preserving anatomical details[15–18]. Finally, deep learning-based methods represent the most recent advancement, using artificial intelligence to automatically detect and correct artifacts, improving image quality with minimal user intervention[19–21]. Although these approaches differ in mechanism and complexity, direct comparisons have been hindered by the absence of standardized evaluation protocols. Our algorithm-independent quantification method addresses this gap by providing a reproducible platform for benchmarking MAR performance across diverse algorithms, exposure settings, and system configurations.

Despite these promising outcomes, this study has some limitations that warrant further investigation. First, the analysis focused on a specific MAR algorithm integrated within a single CBCT system, and performance may vary with other CBCT systems or MAR algorithms, particularly those utilizing advanced deep learning techniques. Comparative studies with other commercially available MAR algorithms and CBCT devices are needed to gain a broader understanding of their relative performance.

Second, although a homogeneous PMMA layer was used as the reference region for thresholding and binarization, this approach may not fully replicate the variability encountered in clinical settings. In real-world practice, the heterogeneity of anatomical structures and metal artifact intensity can complicate the selection of a consistent reference region. Future research should focus on developing automated, universally applicable methods for reference region selection to ensure consistent and reliable results in both clinical and research settings.

Lastly, although we quantitatively assessed the reduction in artifact area, diagnostic accuracy or interpretability was not evaluated. Since artifact reduction does not always equate to improved diagnostic performance, further studies linking quantitative artifact metrics with clinical outcomes will be necessary to fully assess the value of MAR algorithms in practice.

In conclusion, this study quantitatively assessed the performance of a MAR algorithm in CBCT using a standardized quality assurance phantom. The algorithm effectively reduced artifacts across various exposure settings and metal rod orientations. These findings highlight the value of a threshold-based, objective evaluation method and provide a reproducible framework for optimizing and benchmarking MAR techniques.

Data availability

The datasets reported are available upon reasonable request to the corresponding author.

Received: 19 December 2024; Accepted: 19 June 2025
Published online: 01 July 2025

References

1. Washio, H. et al. Metal artifact reduction using iterative CBCT reconstruction algorithm for head and neck radiation therapy: A phantom and clinical study. *Eur. J. Radiol.* **132**, 109293. https://doi.org/10.1016/j.ejrad.2020.109293 (2020).
2. Korpics, M. et al. Observer evaluation of a metal artifact reduction algorithm applied to head and neck cone beam computed tomographic images. *Int. J. Radiat. Oncol. Biol. Phys.* **96**, 897–904 (2016).
3. Zhang, Y. et al. Reducing metal artifacts in cone-beam CT images by preprocessing projection data. *Int. J. Radiat. Oncol. Biol. Phys.* **67**, 924–932 (2007).
4. Shahmirzadi, S. et al. Assessment of the efficiency of a pre- versus post-acquisition metal artifact reduction algorithm in the presence of 3 different dental implant materials using multiple CBCT settings: An in vitro study. *Imaging Sci. Dent.* **51**, 1–7 (2021).
5. Kim, Y. H. et al. Quantitative analysis of metal artifact reduction using the auto-edge counting method in cone-beam computed tomography. *Sci. Rep.* **10**, 8872. https://doi.org/10.1038/s41598-020-65644-3 (2020).
6. Sheikhi, M., Behfarnia, P., Mostajabi, M. & Nasri, N. The efficacy of metal artifact reduction (MAR) algorithm in cone-beam computed tomography on the diagnostic accuracy of fenestration and dehiscence around dental implants. *J. Periodontol.* **91**, 209–214 (2020).
7. Queiroz, P. M., Groppo, F. C., Oliveira, M. L., Haiter-Neto, F. & Freitas, D. Q. Evaluation of the efficacy of a metal artifact reduction algorithm in different cone beam computed tomography scanning parameters. *Oral Surg. Oral Med. Oral Pathol. Oral Radiol.* **123**, 729–734 (2017).
8. Vasconcelos, K. D. F. et al. The performance of metal artifact reduction algorithms in cone beam computed tomography images considering the effects of materials, metal positions, and fields of view. *Oral Surg. Oral Med. Oral Pathol. Oral Radiol.* **127**, 71–76 (2019).
9. Katsura, M., Sato, J., Akahane, M., Kunimatsu, A. & Abe, O. Current and novel techniques for metal artifact reduction at CT: Practical guide for radiologists. *Radiographics* **38**, 450–461 (2018).
10. Barrett, J. F. & Keat, N. Artifacts in CT: Recognition and avoidance. *Radiographics* **24**, 1679–1691 (2004).
11. Kalender, W. A., Hebel, R. & Ebersberger, J. Reduction of CT artifacts caused by metallic implants. *Radiology* **164**, 576–577 (1987).
12. Glover, G. H. & Pelc, N. J. An algorithm for the reduction of metal clip artifacts in CT reconstructions. *Med. Phys.* **8**, 799–807 (1981).
13. Yu, L. et al. Metal artifact reduction from reformatted projections for hip prostheses in multislice helical computed tomography: Techniques and initial clinical results. *Invest. Radiol.* **44**, 691–696 (2009).
14. Chen, L., Liang, Y., Sandison, G. A. & Rydberg, J. A novel method for reducing high attenuation object artifacts in CT reconstructions. *Proc. SPIE Int. Soc. Opt. Eng.* **4684**, 841–850 (2002).
15. Boudabbous, S. et al. Model-based iterative reconstruction (MBIR) for the reduction of metal artifacts on CT. *AJR Am. J. Roentgenol.* **205**, 380–385 (2015).
16. Wang, G., Snyder, D. L., O'Sullivan, J. A. & Vannier, M. W. Iterative deblurring for CT metal artifact reduction. *IEEE Trans. Med. Imaging* **15**, 657–664 (1996).
17. Wang, G., Vannier, M. W. & Cheng, P. C. Iterative X-ray cone-beam tomography for metal artifact reduction and local region reconstruction. *Microsc. Microanal.* **5**, 58–65 (1999).

18. Wang, G., Frei, T. & Vannier, M. W. Fast iterative algorithm for metal artifact reduction in X-ray CT. *Acad. Radiol.* **7**, 607–614 (2000).
19. Kim, S., Ahn, J., Kim, B., Kim, C. & Baek, J. Convolutional neural network–based metal and streak artifacts reduction in dental CT images with sparse-view sampling scheme. *Med. Phys.* **49**, 6253–6277 (2022).
20. Koetzier, L. R. et al. Deep learning image reconstruction for CT: Technical principles and clinical prospects. *Radiology* **306**, e221257. https://doi.org/10.1148/radiol.221257 (2023).
21. Njiti, M. M., Osman, N. D., Mansor, M. S., Rabaiee, N. A. & Abdul Aziz, M. Z. Potential of metal artifact reduction (MAR) and deep learning-based reconstruction (DLR) algorithms integration in CT metal artifact correction: A review. *Radiat. Phys. Chem.* **218**, 111541. https://doi.org/10.1016/j.radphyschem.2024.111541 (2024).

Acknowledgements

This work was supported by the National Research Foundation of Korea (NRF) grant funded by the Korean government (MSIT) (Grant number: RS-2022-NR068890).

Author contributions

G.D. Jo and S.S. Han conceived and designed this study. C.W. Park and G.D. Jo conducted the experiments and analyzed the data. G.D. Jo and K.J. Jeon wrote the first draft of the manuscript. S.S. Han supervised the study and critically reviewed the manuscript. All authors have substantially contributed to the work, reviewed, and approved the final version for submission.

Declarations

Competing interest

The authors declare no competing interests.

Additional information

Correspondence and requests for materials should be addressed to S.-S.H.